# Discovery of Yield Functions in Plasticity via Physics-Informed Convex Neural Networks

Hyeonbin Moon [1], Jecheon Yu [1] and Seunghwa Ryu[1*]

[1]Department of Mechanical Engineering, Korea Advanced Institute of Science and Technology (KAIST), 291 Daehak-ro, Yuseong-gu, Daejeon 34141, Republic of Korea

[*]Corresponding author e-mail

ryush@kaist.ac.kr (Seunghwa Ryu)

**Abstract**

This study presents a physics-informed framework for discovering elasto-plastic yield functions directly from full-field displacement measurements and reaction force data, without relying on stress observations or predefined parametric forms. The yield function is modeled using a convex neural network explicitly designed to satisfy convexity and positive homogeneity of degree one, consistent with rate-independent plasticity theory. The network is embedded within a finite element discretization and trained by minimizing the residuals of the force balance equations across multiple loading scenarios. An explicit stress integration scheme is employed to enable gradient-based optimization while preserving physical consistency. The method is validated on three benchmark yield models—von Mises, Hill 1948, and Yld2000-2d—and is shown to accurately reconstruct both isotropic and anisotropic yield surfaces from a limited set of synthetic tests. To enable deployment in standard implicit solvers, the trained neural yield function is post-processed by fitting it to a smooth polynomial surrogate, which is successfully incorporated into return-mapping–based finite element simulations. These results demonstrate that the proposed approach provides a robust and generalizable pathway for data-driven identification of elasto-plastic constitutive behavior.

Keywords: Deep learning; Physics-informed neural network; Constitutive models; Plasticity; Inverse problems

## 1. Introduction

Constitutive modeling plays a central role in solid mechanics by enabling predictive simulations of material behavior under mechanical loading [1-3]. In particular, plasticity models are essential for describing irreversible deformations under complex, multiaxial loading conditions. A classical elasto-plastic constitutive framework comprises three fundamental components: the yield function, which defines the boundary between elastic and plastic states in stress space; the hardening law, which governs the evolution of the yield surface; and the flow rule, which determines the direction of plastic strain. Among these, the yield function plays a pivotal role, as it governs the onset of plastic deformation and controls the subsequent evolution of plastic flow. Classical models such as the von Mises and Tresca criteria offer robust and interpretable descriptions for isotropic metals under simple loading conditions [4–6]. To capture anisotropy in textured materials and sheet metals, more advanced yield criteria— such as Hill's quadratic yield model and non-quadratic anisotropic yield functions developed by Barlat and Yoon—have been developed [7–12]. These models incorporate additional directional parameters to improve prediction under anisotropic loading. However, their fixed analytical forms remain limited in flexibility and often fail to capture complex yielding behavior, particularly in materials exhibiting strong anisotropy under multiaxial stress states [13,14].

Recent advances in data-driven modeling have introduced alternative approaches for representing complex plastic behavior [15,16]. Neural networks, in particular, have been employed to approximate the full elasto-plastic stress–strain response using synthetic or experimental data, without relying on predefined constitutive forms [17–20]. Feedforward and recurrent architectures have demonstrated the ability to learn path-dependent and rate-dependent responses from strain histories [21,22]. Although these models are capable of

capturing complex responses, they are fundamentally black-box in nature and lack interpretability or correspondence with classical constitutive theory. Specifically, they do not encode internal constitutive components—such as yield functions, flow rules, or hardening behavior—in an explicit or physically consistent manner. Consequently, their use in simulation pipelines is limited, and their generalization across unseen loading paths remains challenging.

To address these limitations, recent studies have explored more interpretable and physics-informed approaches to constitutive model discovery. Rather than treating the stress–strain relation as a direct input–output mapping, these methods aim to identify internal constitutive structures such as yield functions and hardening laws. Symbolic regression frameworks, for example, derive closed-form expressions by fitting to stress–strain data or neural outputs, allowing the discovered models to retain physical meaning and analytical tractability [26–28]. The EUCLID framework (Efficient Unsupervised Constitutive Law Identification and Discovery) poses the identification problem as sparse regression over a set of candidate functions, trained to minimize equilibrium residuals using only displacement and reaction force data [29–31]. While these methods improve interpretability and physical consistency, most have been confined to isotropic plasticity, for which parametric representations are relatively simple and well-established on the π-plane. Extending them to anisotropic materials remains challenging—not only due to the increased complexity of directional dependence, but also because no universal analytical representation exists for anisotropic yield functions. Some studies have attempted to directly learn anisotropic yield surfaces by fitting surrogate models to stress states at yield onset [32,33], but such approaches typically require multiaxial yield stress data, which are difficult or impractical to obtain in experiments. As a result, the combination of physics-informed learning and anisotropic yield identification—without relying on stress observations—remains largely unexplored.

In this work, we propose a physics-informed learning framework that identifies both anisotropic yield functions solely from full-field displacement measurements and reaction force data. The yield function is modeled using an input convex neural network [34,35], which is explicitly constructed to satisfy convexity and positive homogeneity of degree one—two mathematically and physically motivated properties that are essential for ensuring consistency with rate-independent plasticity. The network is trained to minimize the residuals of the force equilibrium equations, which are computed via a finite element discretization of the specimen domain under multiple loading scenarios. Unlike prior methods, which typically focus on either isotropic behavior or rely on direct stress observations, the proposed approach enables the reconstruction of complex anisotropic yield surfaces in a data-efficient manner using only experimentally accessible quantities. Furthermore, the trained neural yield function is post-processed into a smooth polynomial surrogate to ensure compatibility with implicit return-mapping schemes. Validation on three benchmark yield models—von Mises, Hill 1948, and Yld2000-2d—demonstrates that the proposed method accurately reconstructs both isotropic and anisotropic yield surfaces, offering a general and practical framework for data-driven constitutive modeling, compatible with return-mapping-based finite element implementations.

The remainder of the paper is organized as follows. **Section 2** presents the problem formulation, including constitutive assumptions and available data. **Section 3** describes the proposed learning framework, covering the input convex neural network, finite element discretization, and training strategy. **Section 4** reports numerical results on benchmark yield models. **Section 5** discusses post-processing into a smooth analytic form for simulation use. **Section 6** concludes the paper.

## 2. Problem statement

The objective of this study is to identify the yield function that governs the elasto-plastic behavior of a material using a limited set of experimentally accessible measurements. As illustrated in **Fig. 1(a)**, the available data consist of (i) full-field displacement fields obtained via digital image correlation (DIC) and (ii) total reaction force curves measured during mechanical testing. Internal stress measurements are not assumed to be available. The problem is formulated as an inverse identification task: given time-resolved displacement and force data under multiple loading conditions, the goal is to infer a yield function that faithfully reproduces the observed plastic response.

We consider a rate-independent, pressure-insensitive, tension–compression symmetric plasticity model under small deformation and plane stress conditions. The material is assumed to exhibit linear elastic behavior prior to yielding, with a known elastic stiffness tensor $\boldsymbol{C_{el}}$, and to follow an associated flow rule with a known isotropic hardening law (e.g., pre-calibrated from a uniaxial tensile test). The constitutive response is characterized by a scalar-valued yield function $\bar{\sigma} : \mathbb{R}^3 \to \mathbb{R}^1$, which maps the in-plane stress components $(\sigma_{xx}, \sigma_{yy}, \sigma_{xy})$ to an equivalent stress $\sigma_{eq} = \bar{\sigma}(\boldsymbol{\sigma})$. Plastic yielding occurs when the equivalent stress reaches the hardening-dependent yield stress $\rho(\bar{\varepsilon}^p)$, which $\bar{\varepsilon}^p$ denotes the accumulated equivalent plastic strain. The plasticity model follows the standard form:

$$f(\boldsymbol{\sigma}, \bar{\varepsilon}^p) = \bar{\sigma}(\boldsymbol{\sigma}) - \rho(\bar{\varepsilon}^p) \leq 0 \tag{1a}$$

subject to the Kuhn–Tucker conditions:

$$\dot{\bar{\varepsilon}}^p \geq 0, \qquad f \leq 0, \qquad \dot{\bar{\varepsilon}}^p \cdot f = 0 \tag{1b}$$

and the associated flow rule:

$$\dot{\boldsymbol{\varepsilon}}^p = \dot{\bar{\varepsilon}}^p \frac{\partial \bar{\sigma}(\boldsymbol{\sigma})}{\partial \boldsymbol{\sigma}} \tag{1c}$$

The hardening law $\rho(\bar{\varepsilon}^p)$ is assumed to be known a priori, whereas the equivalent stress function $\bar{\sigma}(\boldsymbol{\sigma})$, which defines the shape of the yield surface, is the unknown quantity to be identified.

To facilitate the identification of the yield function, we generate a diverse set of mechanical responses by applying four distinct loading conditions to a single specimen geometry, as shown in **Fig. 1(b)**: uniaxial tension in the x-direction (UTx), uniaxial tension in the y-direction (UTy), biaxial tension (BT), and simple shear (SS). The specimen includes two elliptical voids to induce heterogeneous stress distributions across the domain, allowing the displacement and reaction force data to contain a broad range of internal mechanical states. This heterogeneity is particularly important in few-shot experimental settings, where maximizing the information content of each test is critical [36,37]. For each loading scenario, displacement fields are measured at multiple time steps via digital image correlation (DIC), and the corresponding reaction forces are recorded as total forces acting on the boundary. These displacement–force pairs, measured over multiple time steps, inform the identification of the yield surface.

This problem setting closely follows that introduced in the EUCLID framework [29–31], which also aims to identify constitutive behavior using full-field displacement and reaction force data, without relying on internal stress measurements. While EUCLID formulates the problem as sparse regression over a set of candidate functions—primarily targeting isotropic models—the present study adopts a physics-informed neural network framework to address the inverse identification problem, thereby enabling the discovery of a broader class of yield functions, including anisotropic surfaces.

In constructing the yield function, two theoretical requirements are imposed: (i) convexity, which ensures stability and uniqueness of the plastic flow direction in accordance with Drucker's postulate; and (ii) positive homogeneity of degree one, which guarantees scale invariance of the associated flow rule. These properties are fundamental to the consistency of rate-independent plasticity theory and are enforced as constraints within the proposed identification framework.

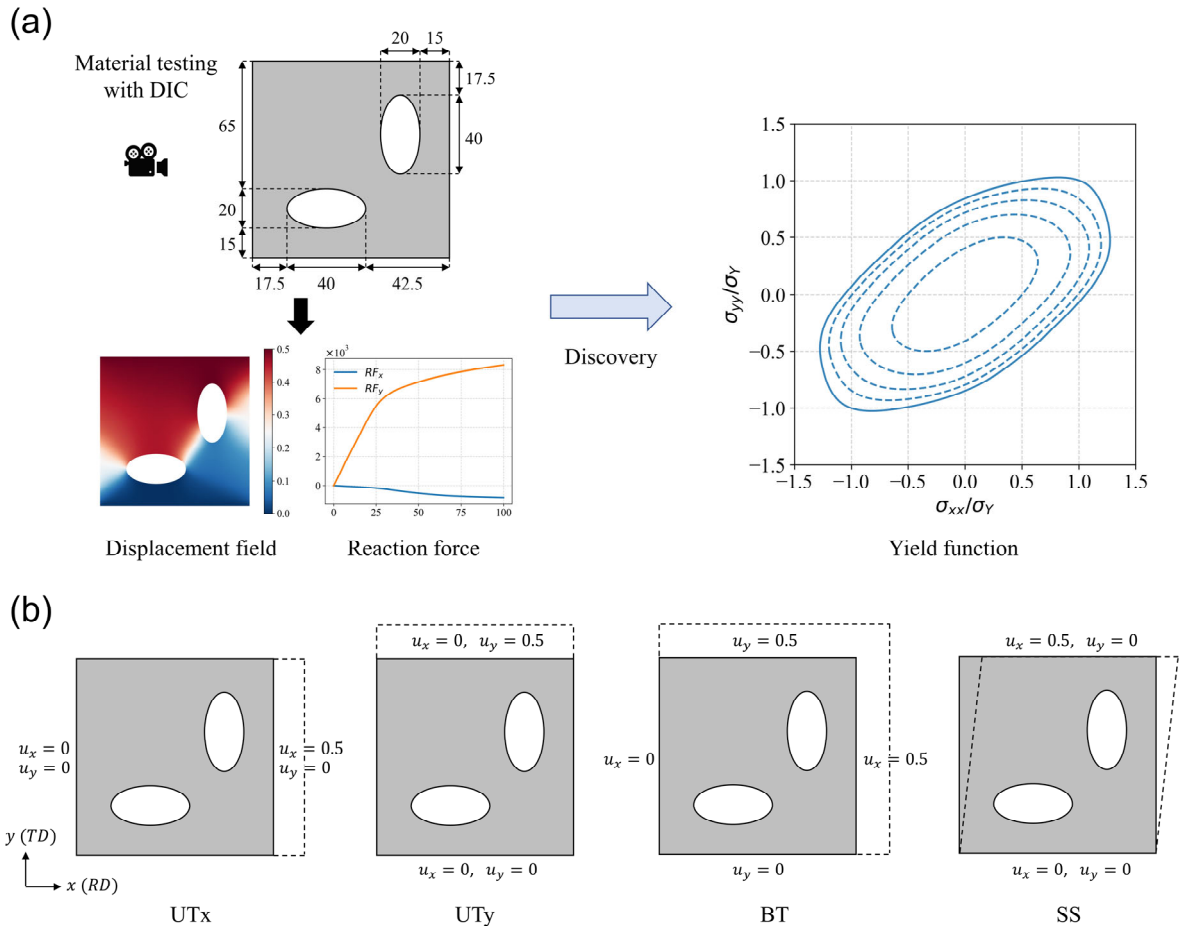


**Fig. 1. Schematic of the problem setup and loading conditions.** (a) Displacement and reaction force data are obtained from mechanical tests using digital image correlation (DIC) and used to identify the yield function. (b) Boundary conditions for the four loading scenarios: uniaxial tension along the x-direction (UTx), uniaxial tension along the y-direction (UTy), biaxial tension (BT), and simple shear (SS). All dimensions are in millimeters.

## 3. Methods

This section outlines the proposed physics-informed learning framework for identifying the yield function. The methodology comprises three main components: (i) representing the yield function using an input convex neural network; (ii) computing the residuals of the force balance equations via finite element discretization; and (iii) training the network by minimizing a physics-based loss derived from an explicit stress integration scheme for rate-independent plasticity. Each component is described in detail in the following subsections.

### 3.1 Convex neural network

To model the yield function $\bar{\sigma}(\boldsymbol{\sigma})$, we adopt a neural network architecture that satisfies two essential structural properties: (i) convexity with respect to the in-plane stress $\boldsymbol{\sigma} = (\sigma_{xx}, \sigma_{yy}, \sigma_{xy})$, and (ii) positive homogeneity of degree one. These properties can be mathematically stated as:

$$(i)\ \ \bar{\sigma}(\theta\boldsymbol{\sigma_1} + (1-\theta)\boldsymbol{\sigma_2}) \leq \theta\bar{\sigma}(\boldsymbol{\sigma_1}) + (1-\theta)\bar{\sigma}(\boldsymbol{\sigma_2})\ \ for\ \ \forall\theta \in [0,1] \qquad (2a)$$

$$(ii)\ \ \bar{\sigma}(\lambda\boldsymbol{\sigma}) = \lambda\bar{\sigma}(\boldsymbol{\sigma})\ \ for\ \ \forall\lambda > 0 \qquad (2b)$$

To enforce convexity, we employ an input convex neural network [34,35], hereafter referred to as a convex neural network. In this architecture, convexity is guaranteed by constraining specific weight matrices to be element-wise non-negative. To ensure positive homogeneity, all bias terms are removed, and the ReLU activation function $s(x) = \max(0, x)$, which is itself positively homogeneous of degree one. This architectural design guarantees that the resulting function is convex and 1-homogeneous by construction. The detailed architecture of the convex neural network is illustrated in **Fig. 2**. The network is composed of multiple hidden layers, each

receiving both the raw stress input and the previous layer's output. The forward pass is defined as:

$$1^{st}\ \text{layer}: \quad \boldsymbol{z_0} = \mathrm{s}(\mathbf{W_0}\boldsymbol{\sigma}), \tag{3a}$$

$$i^{th}\ \text{layer}: \quad \boldsymbol{z_i} = \mathrm{s}\left(\mathbf{W_i^{(\sigma)}}\boldsymbol{\sigma} + \mathbf{W_i^{+}}\boldsymbol{z_{i-1}}\right), \qquad 1 \le i \le \mathrm{N} \tag{3b}$$

where $\boldsymbol{z_i}$ denotes the activation vector of the $i$-th hidden layer. The matrix $\mathbf{W_0}$ and $\mathbf{W_i^{(\sigma)}}$ is an unconstrained weight matrix applied directly to the stress input $\boldsymbol{\sigma}$, while $\mathbf{W_i^{+}}$ is constrained to be element-wise non-negative to ensure convexity. To impose this non-negativity constraint in a differentiable manner, we define each element of $\mathbf{W_i^{+}}$ through a smooth reparameterization:

$$g(x) = \sqrt{x^2 + \gamma^2} - \gamma^2, \qquad \gamma > 0 \tag{4}$$

so that $\mathbf{W_i^{+}} = g(\mathbf{W_i^{raw}})$, where $\mathbf{W_i^{raw}}$ denotes the unconstrained parameter matrix. In this work, we set $\gamma = 0.1$ to balance numerical stability and smoothness during training.

The equivalent stress is approximated by the symmetrized output of the convex neural network:

$$\sigma_{\mathrm{eq}} = \bar{\sigma}(\boldsymbol{\sigma}) \approx NN(\boldsymbol{\sigma}) = NN^{raw}(\boldsymbol{\sigma}) + NN^{raw}(-\boldsymbol{\sigma}) \tag{5}$$

where $NN^{raw}(\boldsymbol{\sigma})$ denotes the output of the original convex neural network prior to symmetrization. This construction ensures tension–compression symmetry, which is a common assumption in pressure-insensitive plasticity models.

It is worth noting that the use of ReLU activation results in a $C^0$-continuous yield function, which lacks the smoothness required for implicit stress integration schemes and

therefore motivates the adoption of an explicit stress integration approach during training, as described in **Section 3.3**.

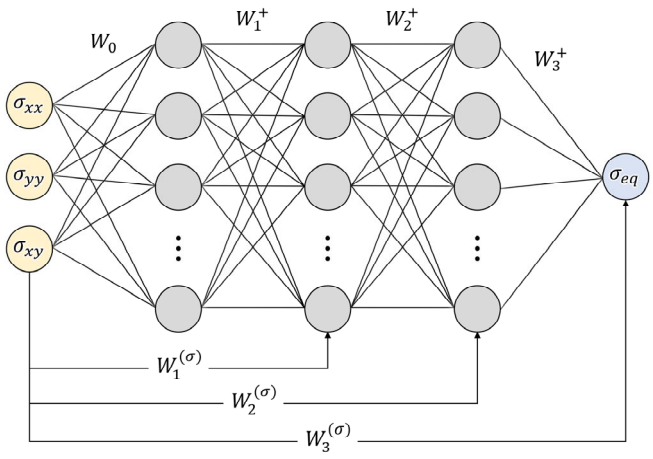


**Fig. 2. Architecture of the convex neural network used to model the yield function.**

### 3.2 Finite element discretization

To compute the strain field from the displacement field and to formulate the governing equations in a numerically tractable form, we adopt a finite element discretization of the computational domain. Our formulation and notation closely follow those introduced in EUCLID [29-31], upon which our implementation is based. The domain Ω is discretized into finite elements, and the displacement field $\boldsymbol{u}(\boldsymbol{x}, t)$ is interpolated using shape functions $N(\boldsymbol{x})$. The corresponding strain field is computed via the strain–displacement relation:

$$\boldsymbol{\varepsilon}(\boldsymbol{x}, t) = \boldsymbol{B}(\boldsymbol{x})\boldsymbol{u_h}(t) \tag{6}$$

where $\boldsymbol{B}(\boldsymbol{x})$ is the strain–displacement matrix derived from the spatial derivatives of the shape functions, and $\boldsymbol{u_h}$ is the vector of nodal displacements at time $t$. Given the availability

of full-field displacement data at multiple time steps, the strain field can be evaluated for each step, and the strain increment $\Delta\boldsymbol{\varepsilon}$ is computed as the difference between successive steps.

To formulate the equilibrium condition, we begin with the weak form of the momentum balance equation under the assumption of negligible body forces:

$$\int_{\Omega} \boldsymbol{\sigma} : \delta\boldsymbol{\varepsilon}\, dV - \int_{\partial\Omega_t} \bar{\mathbf{t}} \cdot \delta\mathbf{u}\, dS = 0 \tag{7}$$

Discretizing Eq. (7) using the finite element method leads to the following algebraic form of the force balance:

$$\boldsymbol{F^{int}} = \int_{\Omega} \boldsymbol{B^T \sigma}\, dV, \qquad \boldsymbol{F^{ext}} = \int_{\partial\Omega_t} N^T \bar{\mathbf{t}}\, dS, \qquad \boldsymbol{F^{int} - F^{ext}} = 0 \tag{8}$$

In incremental form, evaluated between time steps $t_{n-1}$ and $t_n$, the equilibrium equation becomes:

$$\Delta\boldsymbol{F^{int}} = \int_{\Omega} \boldsymbol{B^T} \Delta\boldsymbol{\sigma}\, dV, \qquad \Delta\boldsymbol{F^{ext}} = \int_{\partial\Omega_t} N^T \Delta\bar{\mathbf{t}}\, dS, \qquad \Delta\boldsymbol{F^{int}} - \Delta\boldsymbol{F^{ext}} = 0 \tag{9}$$

In our problem setting, the total reaction force is available only at a subset of boundary nodes where external loads are applied, referred to as the fixed set, while the remaining boundary nodes constitute the free set. To account for this distinction, the internal and external nodal force vectors are partitioned such that force values are retained individually for nodes in the free set, whereas the fixed set is reduced to global force components by summing the nodal contributions in each coordinate direction:

$$\Delta\boldsymbol{F^{int}} = \begin{bmatrix} \Delta\boldsymbol{F^{int}_{free}} \\ \Delta\boldsymbol{F^{int}_{fix}} \end{bmatrix}, \qquad \Delta\boldsymbol{F^{ext}} = \begin{bmatrix} \mathbf{0} \\ \Delta\boldsymbol{F^{ext}_{fix}} \end{bmatrix} \tag{10}$$

The external force on the free set vanishes due to the absence of prescribed tractions or body forces. The external force on the fixed set, $\Delta \boldsymbol{F}_{\boldsymbol{fix}}^{\boldsymbol{ext}}$, is computed as the difference in measured reaction forces between time steps. The corresponding internal force $\Delta \boldsymbol{F}_{\boldsymbol{fix}}^{\boldsymbol{int}}$ is obtained by aggregating internal nodal forces over the fixed set. As a result, both quantities represent global force components and can be directly compared. Based on this partitioning, the incremental residual of the force balance at time step $t_n$ is defined as:

$$R(t_n) = \left\| \Delta \boldsymbol{F}_{\boldsymbol{free}}^{\boldsymbol{int}} \right\|^2 + \left\| \Delta \boldsymbol{F}_{\boldsymbol{fix}}^{\boldsymbol{int}} - \Delta \boldsymbol{F}_{\boldsymbol{fix}}^{\boldsymbol{ext}} \right\|^2 \tag{11}$$

This residual quantifies the deviation from mechanical equilibrium at step $t_n$, and serves as the principal physics loss term in the training framework introduced in **Section 3.3**. A detailed derivation of this formulation is provided in EUCLID [29-31].

### 3.3 Physics-informed learning

To identify the yield function modelled by the convex neural network, we employ a physics-informed training framework based on minimizing the residual of the finite element equilibrium equations introduced in **Section 3.2**. At each time step $t_n$, the strain increment $\Delta \boldsymbol{\varepsilon}(t_n)$ is directly obtained from the full-field displacement data, whereas the corresponding stress increment $\Delta \boldsymbol{\sigma}(t_n)$ is not observed and therefore needs to be inferred.

To this end, we adopt an explicit stress integration scheme based on the forward Euler method. This approach updates the stress using the known strain increment and relies on the yield function $\bar{\sigma}(\boldsymbol{\sigma})$ and its gradient, both provided by the convex neural network. The explicit scheme is particularly appropriate in this setting, as the ReLU-activated neural network yields only $C^0$-continuity and does not provide the smoothness required for computing consistent

tangent operators in implicit methods such as the backward Euler scheme. By avoiding second-order derivatives and iterative procedures, the explicit formulation remains compatible with gradient-based optimization and facilitates stable training.

The stress update begins with the elastic trial step:

$$\boldsymbol{\sigma}^{tr} = \boldsymbol{\sigma}(t_{n-1}) + \boldsymbol{C_{el}}\colon \Delta\boldsymbol{\varepsilon}(t) \tag{12}$$

Plastic yielding is evaluated by comparing the trial equivalent stress $\bar{\sigma}(\boldsymbol{\sigma}^{tr})$ to the current yield threshold $\rho\left(\bar{\varepsilon}^{p}(t_{n-1})\right)$ using a binary indicator function $H$:

$$H = \begin{cases} 1, & \bar{\sigma}(\boldsymbol{\sigma}^{tr}) > \rho\left(\bar{\varepsilon}^{p}(t_{n-1})\right) \\ 0, & otherwise \end{cases} \tag{13}$$

Based on this indicator, the equivalent plastic strain increment and consistent tangent modulus are given by:

$$\Delta\bar{\varepsilon}^{p} = H\frac{\frac{\partial\bar{\sigma}}{\partial\boldsymbol{\sigma}}\colon\boldsymbol{C}_{el}\colon\Delta\boldsymbol{\varepsilon}}{\frac{d\rho}{d\bar{\varepsilon}^{p}} + \frac{\partial\bar{\sigma}}{\partial\boldsymbol{\sigma}}\colon\boldsymbol{C}_{el}\colon\frac{\partial\bar{\sigma}}{\partial\boldsymbol{\sigma}}} \tag{14}$$

$$\boldsymbol{C}_{ep} = \boldsymbol{C}_{el} - H\frac{\left(\boldsymbol{C}_{el}\colon\frac{\partial\bar{\sigma}}{\partial\boldsymbol{\sigma}}\right)\otimes\left(\boldsymbol{C}_{el}\colon\frac{\partial\bar{\sigma}}{\partial\boldsymbol{\sigma}}\right)}{\frac{d\rho}{d\bar{\varepsilon}^{p}} + \frac{\partial\bar{\sigma}}{\partial\boldsymbol{\sigma}}\colon\boldsymbol{C}_{el}\colon\frac{\partial\bar{\sigma}}{\partial\boldsymbol{\sigma}}} \tag{15}$$

However, the binary indicator function $H$ is inherently discontinuous, which is incompatible with gradient-based optimization. To resolve this, we introduce a differentiable approximation using a sigmoid function:

$$\widehat{H} = Sigmoid\left(\beta * \left(NN(\boldsymbol{\sigma}^{tr}) - \rho\left(\bar{\varepsilon}^{p}(t_{n-1})\right)\right)\right) \tag{16}$$

where $\beta$ controls the sharpness of the transition. As $\beta \to \infty$, the smoothed indicator $\widehat{H}$ converges to the original step function $H$, as illustrated in **Fig. 3**. By incorporating the

smoothed indicator and using the neural approximation $\bar{\sigma}(\boldsymbol{\sigma}) \approx NN(\boldsymbol{\sigma})$ from Eq. (5), the equivalent plastic strain increment becomes:

$$\Delta\bar{\varepsilon}^{p} = \widehat{H}\frac{\frac{\partial NN}{\partial \boldsymbol{\sigma}} : \boldsymbol{C}_{el} : \Delta\boldsymbol{\varepsilon}}{\frac{d\rho}{d\bar{\varepsilon}^{p}} + \frac{\partial NN}{\partial \boldsymbol{\sigma}} : \boldsymbol{C}_{el} : \frac{\partial NN}{\partial \boldsymbol{\sigma}}} \tag{17}$$

and the corresponding elasto-plastic tangent modulus is given by:

$$\widehat{\boldsymbol{C}}_{ep} = \boldsymbol{C}_{el} - \widehat{H}\frac{\left(\boldsymbol{C}_{el} : \frac{\partial NN}{\partial \boldsymbol{\sigma}}\right) \otimes \left(\boldsymbol{C}_{el} : \frac{\partial NN}{\partial \boldsymbol{\sigma}}\right)}{\frac{d\rho}{d\bar{\varepsilon}^{p}} + \frac{\partial NN}{\partial \boldsymbol{\sigma}} : \boldsymbol{C}_{el} : \frac{\partial NN}{\partial \boldsymbol{\sigma}}} \tag{18}$$

The stress increment is then computed via:

$$\Delta\boldsymbol{\sigma} = \widehat{\boldsymbol{C}}_{ep} : \Delta\boldsymbol{\varepsilon} \tag{19}$$

All quantities required for the stress update—including the neural yield function, its gradient with respect to stress, the hardening law, and its derivative—are computed using the stress and equivalent plastic strain evaluated at the previous time step $t_{n-1}$. Once the stress field is updated, internal forces are assembled through the finite element formulation, and the force residual $R(t_n)$, as defined in Eq. (11), is computed accordingly.

To construct the overall loss function, residuals are accumulated over all time steps and all loading conditions (UTx, UTy, BT, SS). The total physics loss is defined as:

$$L_{physics} = \sum_{k\in\{\mathrm{UTx,UTy,BT,SS}\}} \sum_{n=1}^{N_t} R^{(k)}(t_n) \tag{20}$$

where $N_t$ is the number of time steps used for each loading condition $k$. This loss is minimized using gradient-based optimization to update the parameters of the convex neural

network. A summary of the complete training pipeline including stress integration, residual computation, and parameter update is provided in **Table 1**.

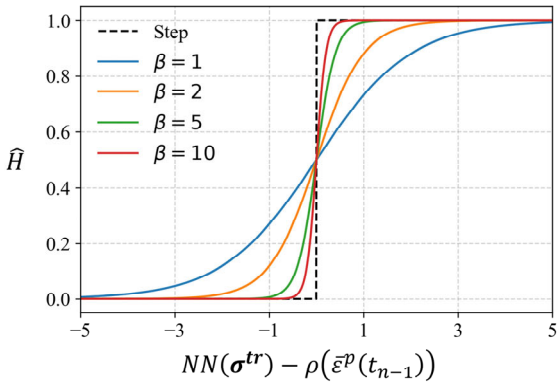


**Fig. 3. Sigmoid approximation of the plasticity indicator for different $\beta$.**

**Table. 1. Physics informed learning framework**

| **Algorithm 1** Training algorithm |
|---|
| 1. Given displacement fields and reaction forces for UTx, UTy, BT, SS |
| 2. Interpolate displacement field and discretize domain by mesh |
| 3. Compute strain increment $\Delta\boldsymbol{\varepsilon}$ of each time steps using shape function |
| 4. Compute external force increment vector $\Delta F_{fix}^{ext}$ of each time steps using reaction forces |
| 5. Initialize loss $L_{physics} = 0$ |
| 6. Evaluate $L_{physics}$ |
| For loading case in {UTx, UTy, BT, SS} |
| Initialize $\bar{\varepsilon}^{p} = 0$, $\boldsymbol{\sigma} = \mathbf{0}$, |
| For t in range(total time steps) |
| Compute trial stress $\boldsymbol{\sigma}^{\boldsymbol{tr}} = \boldsymbol{\sigma} + \boldsymbol{C}_{el}{:}\Delta\boldsymbol{\varepsilon}$ |
| Compute indicator $\widehat{H} = Sigmoid\left(\beta * \left(NN(\boldsymbol{\sigma}^{\boldsymbol{tr}}) - \rho(\bar{\varepsilon}^{p})\right)\right)$ |
| Compute elastoplastic stiffness tensor $\widehat{\boldsymbol{C}}_{ep} = \boldsymbol{C}_{el} - \widehat{H}\frac{\left(\boldsymbol{C}_{el}{:}\frac{\partial NN}{\partial\boldsymbol{\sigma}}\right)\otimes\left(\boldsymbol{C}_{el}{:}\frac{\partial NN}{\partial\boldsymbol{\sigma}}\right)}{\frac{d\rho}{d\bar{\varepsilon}^{p}} + \frac{\partial NN}{\partial\boldsymbol{\sigma}}{:}\boldsymbol{C}_{el}{:}\frac{\partial NN}{\partial\boldsymbol{\sigma}}}$ |
| Compute stress increment $\Delta\boldsymbol{\sigma} = \hat{C}_{ep}{:}\Delta\boldsymbol{\varepsilon}$ |
| Compute equivalent plastic strain increment $\Delta\bar{\varepsilon}^{p} = \frac{\frac{\partial NN}{\partial\boldsymbol{\sigma}}{:}\boldsymbol{C}_{el}{:}\Delta\boldsymbol{\varepsilon}}{\frac{d\rho}{d\bar{\varepsilon}^{p}} + \frac{\partial NN}{\partial\boldsymbol{\sigma}}{:}\boldsymbol{C}_{el}{:}\frac{\partial NN}{\partial\boldsymbol{\sigma}}}$ |
| Compute nodal internal force increment vector $\Delta F^{int} = \iint B^{T}\Delta\boldsymbol{\sigma}\,dxdy$ |
| Update Loss $L_{physics} \leftarrow L_{physics} + \left\|\Delta F_{free}^{int}\right\|^{2} + \left\|\Delta F_{fix}^{int} - \Delta F_{fix}^{ext}\right\|^{2}$ |
| Update stress $\boldsymbol{\sigma} \leftarrow \boldsymbol{\sigma} + \Delta\boldsymbol{\sigma}$ |
| Update equivalent plastic strain $\bar{\varepsilon}^{p} \leftarrow \bar{\varepsilon}^{p} + \Delta\bar{\varepsilon}^{p}$ |
| 7. Backpropagation and update convex neural network $NN$ parameters |
| 8. Repeat 6 & 7 until loss converge |

## 4. Results

This section presents the results of the proposed physics-informed learning framework applied to benchmark problems with known yield functions. All training and evaluation are conducted on synthetic data generated from finite element simulations, where ground-truth yield functions are prescribed. All simulations and training are performed under consistent hyperparameter and implementation settings, as summarized below.

The computational domain is discretized using 8,876 linear triangular elements. The yield function is represented by an input convex neural network comprising three hidden layers, each with 64 neurons and ReLU activation functions. The network is trained for 1,000 epochs using the Adam optimizer with a learning rate of $10^{-3}$. To enable a smooth transition from elastic to plastic behavior, the sharpness parameter $\beta$ in the sigmoid-based plasticity indicator $\widehat{H}$ is progressively increased during training: $\beta = 2$ for epochs 0–200, $\beta = 4$ for epochs 200–400, $\beta = 6$ for epochs 400–600, $\beta = 8$ for epochs 600–800, and $\beta = 10$ for the final 200 epochs. This staged schedule facilitates convergence by gradually approximating the ideal step function behavior of the plasticity indicator.

### 4.1 Data generation

To evaluate the proposed framework, synthetic data are generated using finite element simulations with predefined ground-truth yield models. Three benchmark yield functions are considered: the isotropic von Mises model, Hill's 1948 anisotropic quadratic model (Hill1948), and the anisotropic non-quadratic Yld2000-2d model. The analytical forms and corresponding parameters of these models are provided in **Appendix A**, and their normalized yield surfaces are illustrated in **Fig. 4**. These benchmarks span a range of complexity, enabling a systematic

assessment of the framework's ability to recover both isotropic and anisotropic yield behavior without assuming any particular parametric structure.

All simulations are performed under plane stress conditions using the commercial finite element package Abaqus, with a user-defined material subroutine (UMAT). The computational domain, discretized into 8,876 linear triangular elements, includes two elliptical voids to induce heterogeneous stress distributions. Four distinct loading conditions are applied to the same specimen geometry: uniaxial tension in the x-direction (UTx), uniaxial tension in the y-direction (UTy), biaxial tension (BT), and simple shear (SS). For the anisotropic models (Hill1948 and Yld2000-2d), the x- and y-directions are aligned with the rolling direction (RD) and the transverse direction (TD), respectively, following standard conventions in sheet metal forming.

Each loading case is simulated for 500 time steps using an implicit return mapping scheme based on the backward Euler method. Displacement fields and total reaction forces are extracted every 5 time steps, resulting in 100 data snapshots per loading condition. This subsampling strategy reflects the practical limitations of DIC-based experimental acquisition and helps reduce computational overhead. To emulate measurement noise, zero-mean Gaussian noise with spatiotemporal correlation is added to the displacement field. Correlation lengths are set to 5 mm in space and 5 steps in time. The noise is normalized on a per-frame basis and scaled to magnitudes of 0.1μm, 0.2μm, or 0.3μm. The 0.1μm level approximates the resolution achievable by modern high-resolution DIC systems [38,39]. Further details on noise generation are provided in **Appendix B**.

All simulations employ the same isotropic elastic properties, with a Young's modulus of $E$ = 69GPa and a Poisson's ratio of $\nu$ = 0.3, and use the same isotropic hardening law:

$$\rho(\bar{\varepsilon}^p) = 417.501(0.00457 + \bar{\varepsilon}^p)^{0.22194} \tag{21}$$

with an initial yield stress of $\sigma_Y = 126.27\text{MPa}$. These parameters are held fixed across all simulations to isolate the effect of the yield surface shape on identification performance.

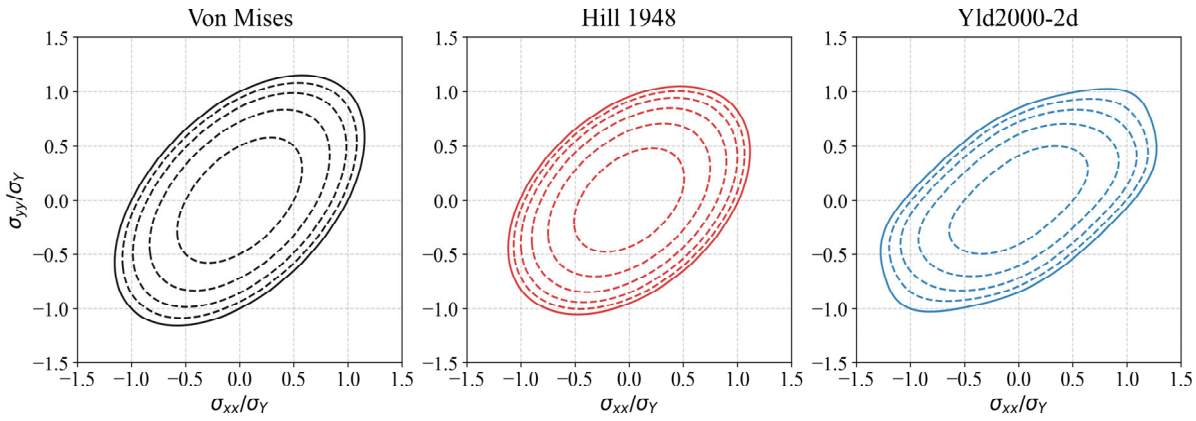


**Fig. 4. Yield surfaces of benchmark models.** (a) von Mises (b) Hill1948 (c) Yld2000-2d

### 4.2 Isotropic benchmark: von Mises

The proposed framework is first evaluated on the isotropic von Mises yield function, which serves as a canonical benchmark in computational plasticity. **Fig. 5(a)** shows the evolution of the physics loss over 1,000 training epochs under noise-free displacement data. The loss is reported separately for each loading case (UTx, UTy, BT, SS), as well as the total loss. As training progresses, the loss decreases consistently, with marked reductions coinciding with each scheduled update of the sigmoid sharpness parameter $\beta$. After $\beta$ reaches its final value of 10 at epoch 800, the loss plateaus, indicating convergence.

The yield surface inferred from the trained convex neural network is presented in **Fig. 5(b)** and compared against the analytical von Mises solution. The contours correspond to

the level set $\bar{\sigma}(\boldsymbol{\sigma}) = \sigma_Y$, extracted from the three-dimensional yield function and visualized as iso-shear lines in the $(\sigma_{xx}, \sigma_{yy})$ plane. The identified yield surface exhibits close agreement with the expected elliptical shape, confirming that the model captures the isotropic nature of the target function. A slight discrepancy is observed near the line $\sigma_{xx} = -\sigma_{yy}$ within the plane $\sigma_{xy} = 0$, which motivates further analysis of the stress states induced in the specimen under each loading condition.

**Fig. 6** shows the spatial distribution of stress states encountered during yielding, as obtained from the ground-truth simulations. For each loading scenario, stress tensors at all integration points that experienced plastic yielding are collected and normalized to lie on the surface $\bar{\sigma}(\boldsymbol{\sigma}) = \sigma_Y$. The aggregated distribution reveals sparse coverage near $\sigma_{xx} = -\sigma_{yy}$, particularly in the $\sigma_{xy} = 0$ plane. This insufficient coverage likely contributes to the localized discrepancy observed in **Fig. 5(b)**, highlighting the importance of applying diverse loading paths to achieve uniform coverage of the stress space.

To evaluate robustness under measurement uncertainty, **Fig. 7** presents results obtained by applying increasing levels of synthetic Gaussian noise to the displacement field: 0.1μm, 0.2μm, and 0.3μm. **Fig. 7(a)** shows that higher noise levels result in slower convergence and increased final physics loss. As shown in **Fig. 7(b)**, the yield surface remains accurately identified at 0.1μm—consistent with the resolution of modern DIC systems—but begins to degrade at 0.2μm and is no longer reliably recovered at 0.3μm. These results indicate that the proposed method remains effective under realistic noise levels, while exhibiting sensitivity to excessive noise.

Finally, **Fig. 8** validates the identified yield function by comparing the predicted and ground truth field quantities at the final loading increment for the UTx case under noise-free conditions. The predicted equivalent stress $\sigma_{eq}$ and equivalent plastic strain $\bar{\varepsilon}^p$ are not

obtained through independent evaluation after training, but are computed incrementally during training as part of the stress update required for evaluating the physics loss. Specifically, the stress field is updated at each time step using the explicit integration scheme, and the equivalent plastic strain is accumulated via the internal variable tracked during training. The predicted fields at the final step ($\beta$ =10) are thus the result of this time-marching process. When compared to the ground-truth solution, the predicted fields show excellent agreement, with discrepancies confined to regions of intense plastic deformation. This confirms that the identified yield surface not only recovers the macroscopic yield geometry, but also enables physically consistent reconstruction of internal field quantities across the domain.

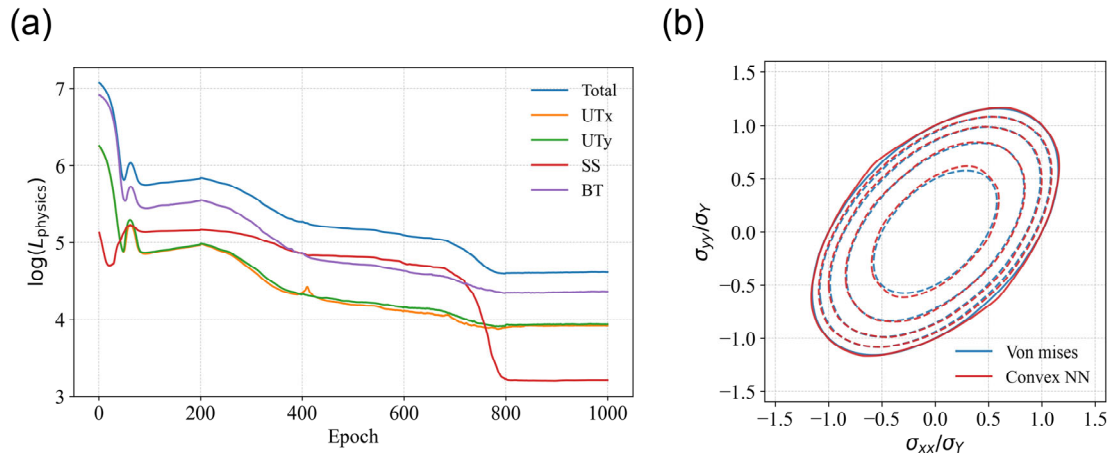


**Fig. 5. Training results for the von Mises benchmark under noise-free conditions.** (a) Physics loss over epochs for each loading condition and total. (b) Comparison of the inferred yield surface and the von Mises solution on the $(\sigma_{xx}, \sigma_{yy})$ plane

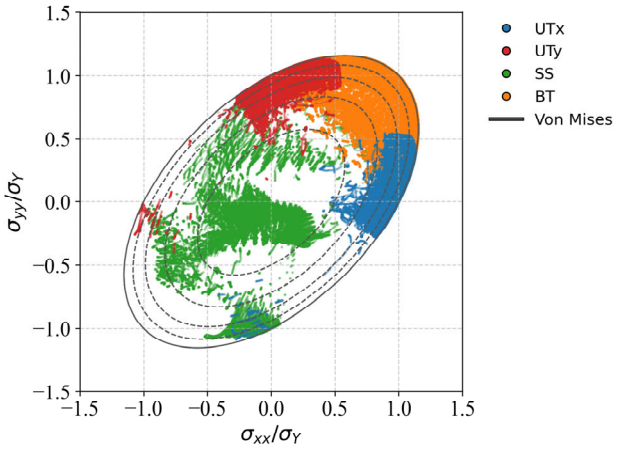


**Fig. 6. Ground-truth stress states at yielding projected onto the von Mises surface.**

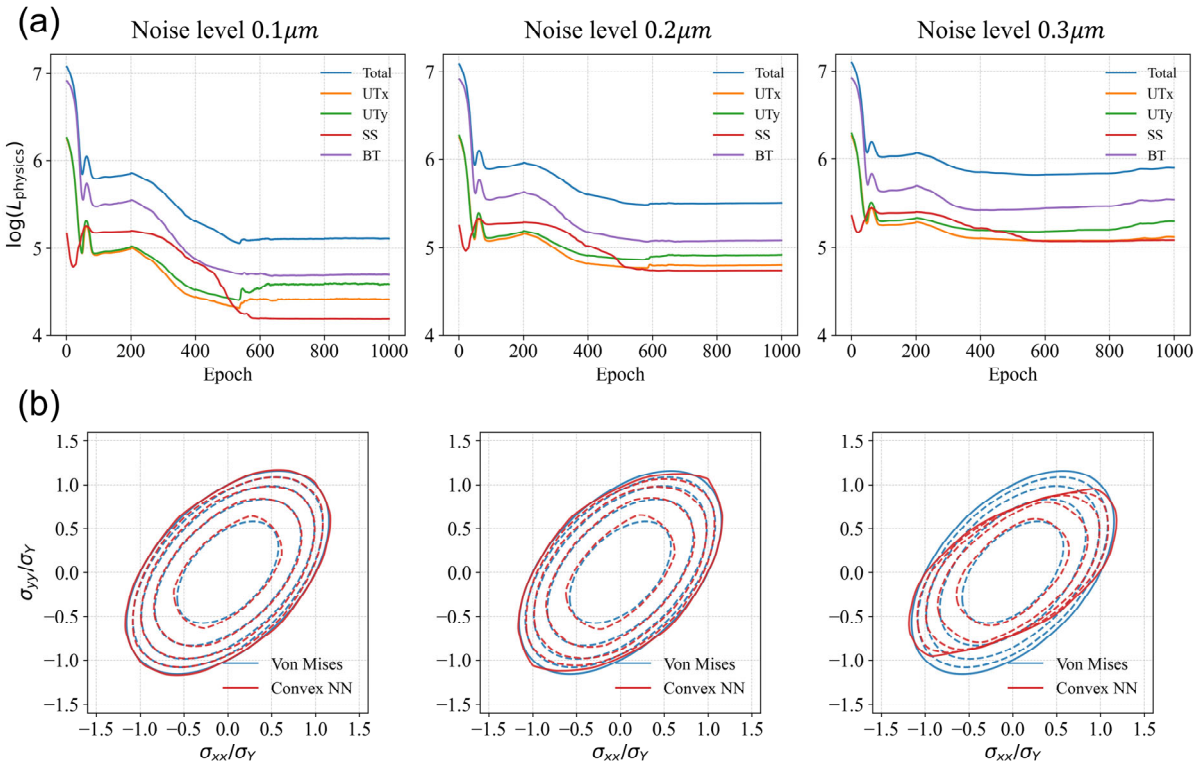


**Fig. 7. Training results for the von Mises benchmark under varying noise levels.** (a) Physics loss over epochs at noise levels of 0.1μm, 0.2μm, and 0.3μm. (b) Comparison of the inferred yield surfaces and the von Mises solution on the $(\sigma_{xx}, \sigma_{yy})$ plane

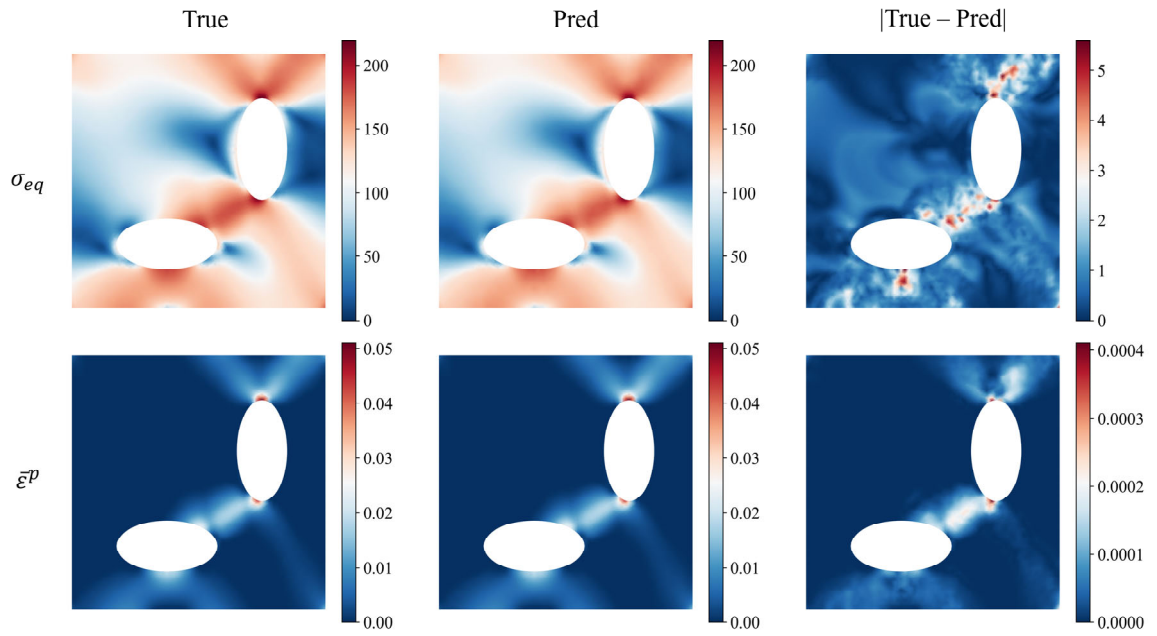


**Fig. 8. Comparison of predicted and ground-truth equivalent stress and strain fields for the von Mises benchmark.** Equivalent stress $\sigma_{eq}$ (top) and equivalent plastic strain $\bar{\varepsilon}^p$(bottom) under UTx loading at the final step. Left: ground truth; middle: model prediction; right: absolute error.

### 4.3 Anisotropic benchmark: Hill1948

The proposed framework is further evaluated using the anisotropic Hill 1948 yield criterion. **Fig. 9** shows the reconstructed yield surfaces obtained from displacement data at different noise levels: noise-free, 0.1μm, 0.2μm, and 0.3μm. The contours represent iso-shear lines corresponding to the level set $\bar{\sigma}(\boldsymbol{\sigma}) = \sigma_Y$, projected onto the $(\sigma_{xx}, \sigma_{yy})$ plane. Under noise-free and 0.1μm conditions, the inferred yield surfaces closely match the ground truth solution. As the noise increases, the inferred surfaces become progressively distorted, with significant deviations observed at 0.3μm. These trends are consistent with the noise sensitivity observed in the von Mises benchmark.

To further examine the model's ability to reproduce directional anisotropy, **Fig. 10** compares the orientation-dependent normalized yield stress $\sigma_\theta/\sigma_{RD}$ and the corresponding r-value derived from the trained yield function. The predicted yield stress profile agrees well with the analytical Hill 1948 model, accurately reflecting the directional variation. The predicted r-value, however, exhibits minor fluctuations superimposed on the correct overall trend. These inconsistencies are attributed to the $C^0$-continuity of the convex neural network. Since the r-value is computed from directional derivatives of the yield surface, the absence of gradient smoothness results in chattering behavior. This illustrates a fundamental trade-off in the network design: while convexity and positive homogeneity are strictly enforced by construction, differentiability is not guaranteed.

**Fig. 11** compares the predicted field distributions of equivalent stress and equivalent plastic strain with those obtained from the ground-truth yield function under the UTx loading condition. The reconstructed fields closely match the ground-truth solution, with discrepancies confined to localized regions of plastic deformation. These results demonstrate that the identified anisotropic yield function enables stable and physically consistent stress integration across the domain, even in the presence of directional yielding.

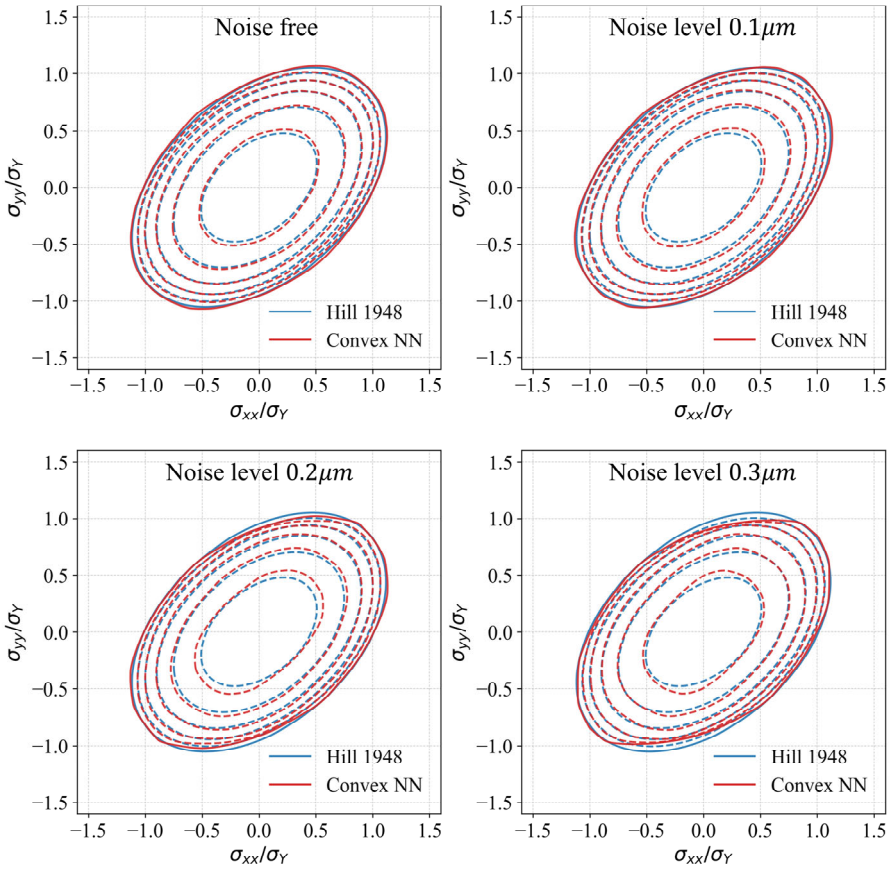


**Fig. 9. Comparison of inferred and analytical yield surfaces for the Hill 1948 benchmark under varying noise levels.** Results are shown for noise levels of 0μm, 0.1μm, 0.2μm, and 0.3μm.

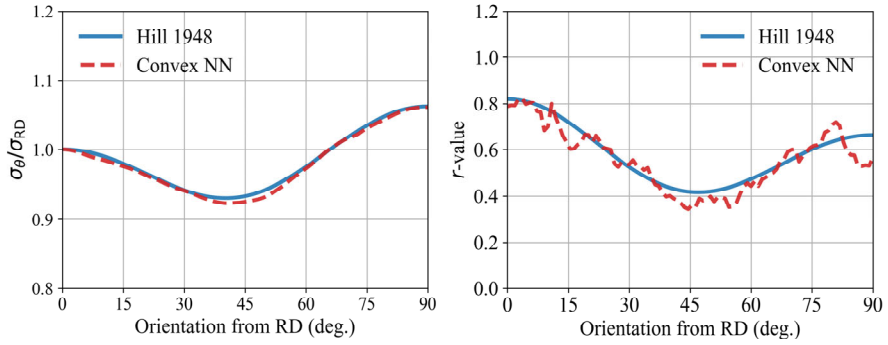


**Fig. 10. Comparison of r-value and normalized yield stress ratio for the Hill 1948 benchmark.**

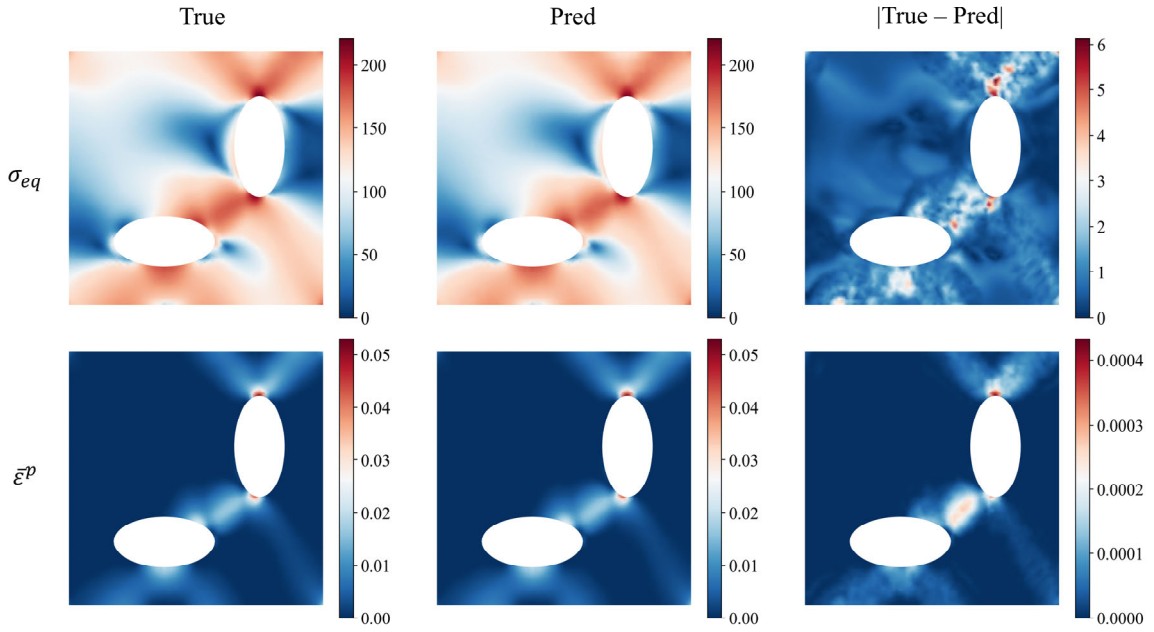


**Fig. 11. Comparison of predicted and ground-truth equivalent stress and strain fields for the Hill 1948 benchmark.** Equivalent stress $\sigma_{eq}$ (top) and equivalent plastic strain $\bar{\varepsilon}^p$(bottom) under UTx loading at the final step. Left: ground truth; middle: model prediction; right: absolute error.

### 4.4 Anisotropic benchmark: Yld2000-2d

The final benchmark evaluates the framework on the Yld2000-2d yield function, a non-quadratic anisotropic criterion widely used in sheet metal forming. **Fig. 12** shows the reconstructed yield surfaces at different noise levels. The predictions align well with the ground-truth geometry under noise-free and 0.1μm conditions, while noticeable distortion emerges at 0.3μm. These results confirm that the method remains robust even for highly nonlinear, non-polynomial yield surfaces.

**Fig. 13** presents the normalized yield stress and r-value profiles extracted from the trained model. The predicted stress profile closely matches the analytical solution, accurately reproducing the directional anisotropy of the Yld2000-2d criterion. Minor deviations in the r-

value are again observed, consistent with the limited smoothness of the convex neural network. **Fig. 14** shows the equivalent stress and equivalent plastic strain fields under the UTx loading condition. The predicted distributions agree well with those generated from the ground-truth yield function, with discrepancies confined to localized plastic regions. These results confirm that the identified yield function supports stable stress integration even for highly anisotropic, non-quadratic surfaces.

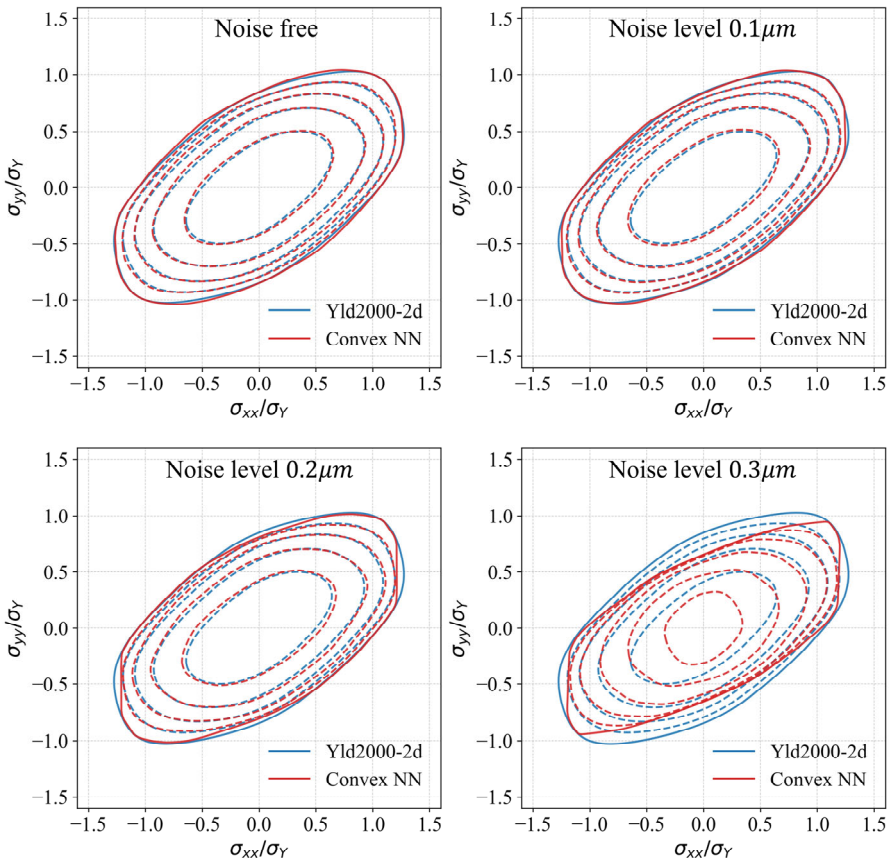


**Fig. 12. Comparison of inferred and analytical yield surfaces for the Yld2000-2d benchmark under varying noise levels.** Results are shown for noise levels of 0μm, 0.1μm, 0.2μm, and 0.3μm.

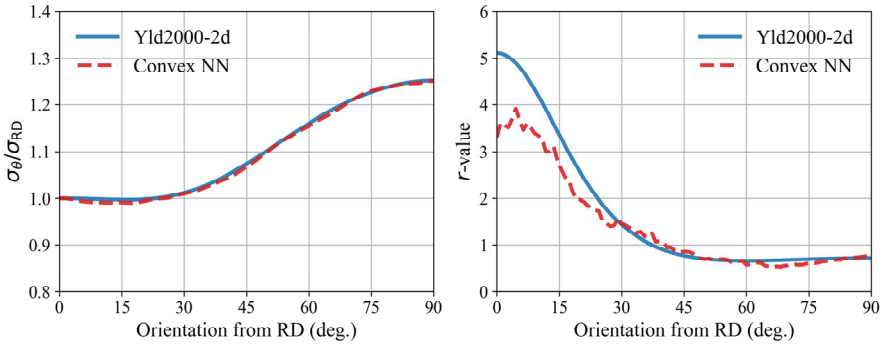


**Fig. 13. Comparison of r-value and normalized yield stress ratio for the Yld2000-2d benchmark.**

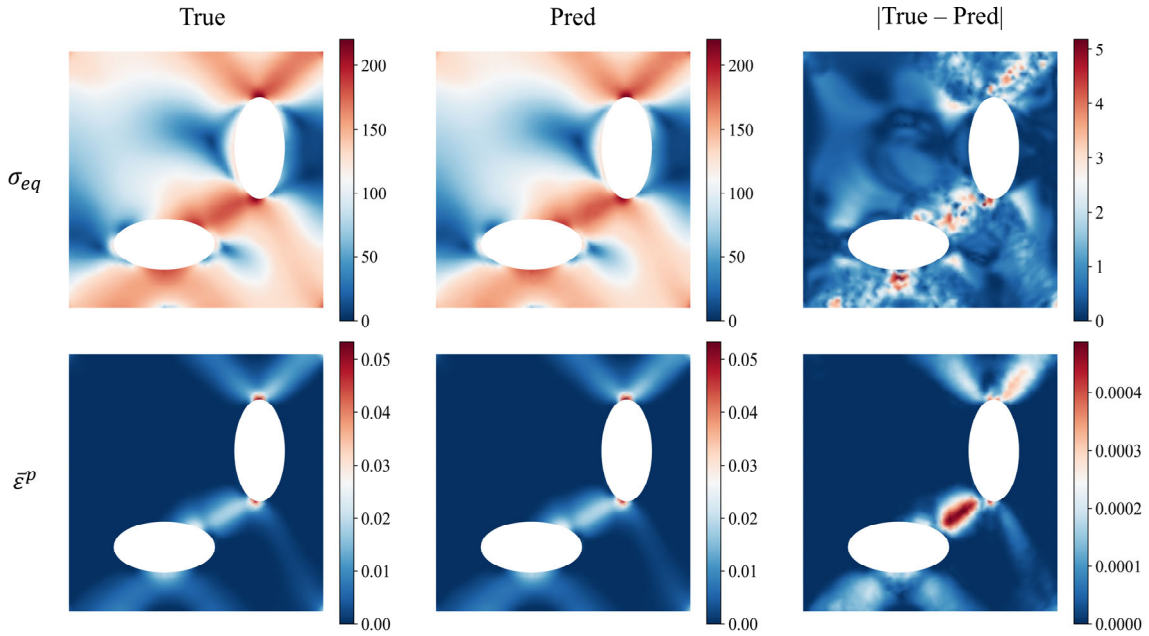


**Fig. 14. Comparison of predicted and ground-truth equivalent stress and strain fields for the Yld2000-2d benchmark.** Equivalent stress $\sigma_{eq}$ (top) and equivalent plastic strain $\bar{\varepsilon}^p$(bottom) under UTx loading at the final step. Left: ground truth; middle: model prediction; right: absolute error.

## 5. Validation

While the trained convex neural network provides a robust and interpretable approximation of the yield surface, its $C^0$-continuity and lack of a closed-form expression limit its direct applicability in standard implicit plasticity algorithms, such as the backward Euler return-mapping scheme, which typically require yield functions with at least $C^1$-smoothness to ensure well-defined derivatives and stable convergence. To address this limitation and enable compatibility with conventional finite element implementations, the neural yield function is post-processed by fitting it to a smooth analytic surrogate. This procedure is demonstrated using the Yld2000-2d model as a representative case.

We adopt a $C^1$-continuous polynomial yield function [40-42] composed of positively homogeneous terms of degrees 2, 4, 6, and 8, defined as:

$$\bar{\sigma}(\boldsymbol{\sigma}) = \sum_{m\in\{2,4,6,8\}} \left( \sum_{i+j+k=m} c_{ijk}^{(m)} \sigma_{xx}^{i} \sigma_{yy}^{j} \sigma_{xy}^{k} \right)^{1/m} \tag{22}$$

where $c_{ijk}^{(m)}$ are the trainable coefficients associated with each homogeneous term of degree $m$. It should be noted that the polynomial representation in Eq. (22) does not guarantee convexity by construction. In contrast to the convex neural network, in which convexity is strictly enforced through the network architecture, the polynomial yield function is obtained through a post-processing fitting procedure and therefore does not possess a strict convexity guarantee. Nevertheless, because the fitting is carried out with respect to a yield surface that is convex by design and the approximation error is maintained at a sufficiently low level, the fitted polynomial is found to closely approximate a convex yield surface. The fitting is performed by minimizing the mean squared error between the polynomial model and the neural network output over 100,000 stress samples uniformly distributed along the level set $\bar{\sigma}(\boldsymbol{\sigma}) =$

$\sigma_Y$. This dense sampling ensures that the fitted polynomial preserves the geometric features of the yield surface discovered by the network. **Fig. 15(a)** shows the convergence of the fitting loss, and **Fig. 15(b)** confirms that the fitted polynomial closely replicates both the neural prediction and the analytical Yld2000-2d surface.

To assess whether the fitted model preserves the physical accuracy of the original yield function, it is incorporated into an implicit return-mapping finite element simulation and evaluated under the UTx loading condition. The resulting distributions of stress and equivalent plastic strain are shown in **Fig. 16** and compared with those obtained using the ground-truth Yld2000-2d model. The predicted fields exhibit strong agreement, with deviations confined to localized plastic zones. These results confirm that the fitted polynomial surrogate accurately reproduces the behavior of the ground-truth model and is suitable for simulation contexts requiring closed-form smoothness.

It is important to note that the adopted polynomial form represents one possible post-processing strategy rather than a uniquely optimal solution. Depending on the application, alternative analytic surrogates—such as those derived via symbolic regression—may also be appropriate. While convex neural networks offer strong expressiveness and structural guarantees by construction, their lack of gradient continuity limits their direct use in implicit schemes. The two-stage approach proposed here—data-driven discovery via convex neural networks followed by analytic fitting—offers a practical and flexible pathway for integrating learned yield surfaces into standard computational plasticity frameworks.

While it is theoretically possible to directly train a polynomial yield function without relying on neural networks, enforcing convexity in polynomial form is nontrivial and typically requires complex mathematical constraints that are difficult to incorporate into a stable optimization process. Moreover, high-degree polynomials often introduce training instability

due to steep gradients and multiple local minima associated with redundant roots. Based on our experience, such models frequently failed to converge and were unable to consistently recover valid convex yield surfaces. In contrast, the convex neural network ensures convexity by architectural design and enables stable and flexible approximation of the yield function. A smooth polynomial surrogate is then fitted to the neural output, providing an analytic representation compatible with standard finite element implementations.

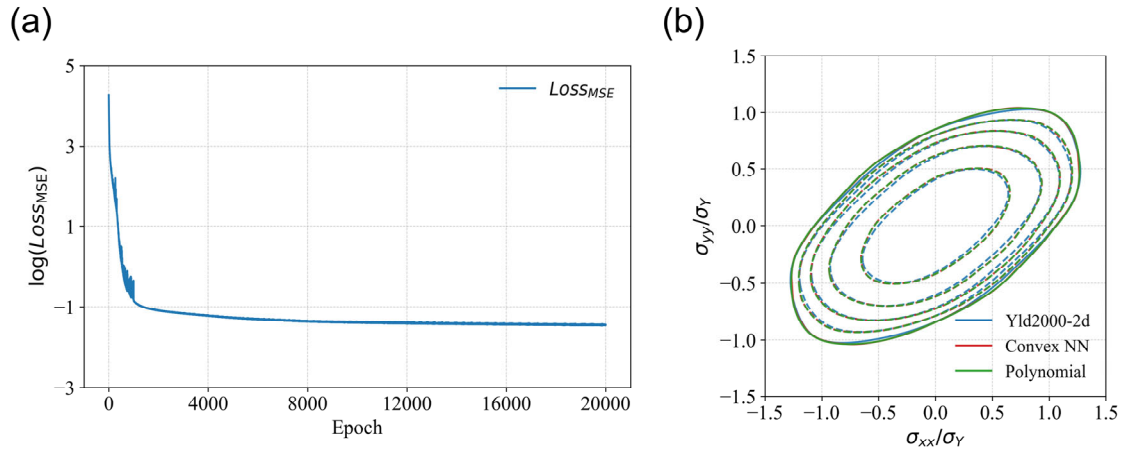


**Fig. 15. Polynomial fitting of the inferred yield function for the Yld2000-2d benchmark.** (a) Convergence of the mean squared error loss over 20,000 fitting epochs. (b) Comparison of the analytical Yld2000-2d surface, convex neural network output, and fitted polynomial on the $(\sigma_{xx}, \sigma_{yy})$ plane

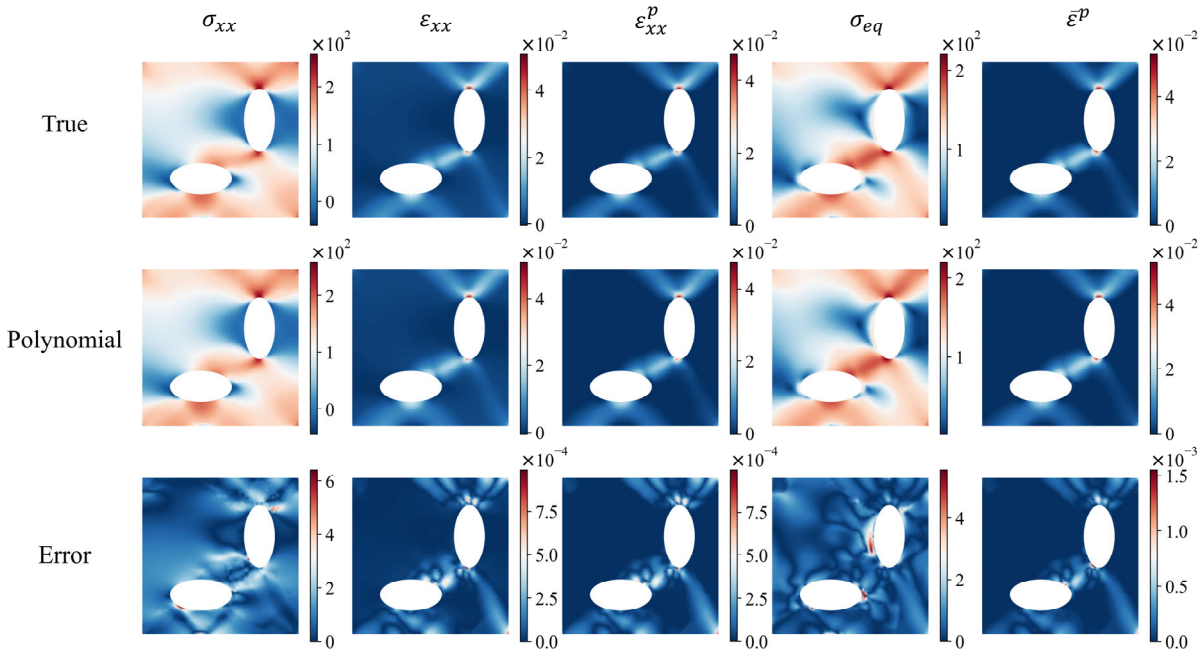


**Fig. 16. Comparison of simulation results using the ground-truth and fitted polynomial yield functions.** Stress, strain, and plasticity fields under UTx loading at the final step. Top: ground truth; middle: fitted polynomial result; bottom: absolute error. The fitted model accurately reproduces the original yield behavior, with discrepancies limited to localized plastic zones.

## 6. Conclusions

This study presented a physics-informed framework for identifying elasto-plastic yield functions directly from full-field displacement fields and reaction force curves, without requiring internal stress measurements or predefined parametric assumptions. The yield function was modeled using a convex neural network architecture that guarantees convexity and positive 1-homogeneity by design. Embedded within a finite element formulation, the network was trained by minimizing the residuals of force equilibrium across multiple loading conditions. An explicit stress integration scheme was employed to ensure compatibility with rate-independent plasticity theory while enabling gradient-based optimization. The proposed approach successfully recovered both isotropic and anisotropic yield surfaces under plane stress, demonstrating its capacity to capture complex material behavior from limited data.

The framework was validated on benchmark models including von Mises, Hill1948, and Yld2000-2d, and was shown to reconstruct the underlying yield surfaces with high fidelity, even in the presence of measurement noise levels representative of modern DIC systems. The trained models reproduced key directional indicators such as the normalized yield stress and captured the overall trend of the r-value without prior knowledge of anisotropy. Moreover, the predicted field quantities—equivalent stress and plastic strain—were in close agreement with those obtained from the ground-truth models, confirming the mechanical consistency of the identified yield functions.

To enable deployment in standard implicit return-mapping solvers, the neural yield surface was post-processed by fitting it to a smooth polynomial surrogate. The resulting analytic representation was successfully incorporated into a finite element simulation, reproducing the target response with high accuracy. While the chosen polynomial form is not unique, the two-stage strategy—data-driven discovery via convex neural networks followed by

analytic fitting—offers a general and effective approach for integrating learned constitutive behavior into simulation-ready plasticity models.

## Declaration of Competing Interest

The authors declare that they have no known competing financial interests or personal relationships that could have appeared to influence the work reported in this paper

## Data availability

Data will be made available on request.

## Acknowledgements

This research was supported by…

**Appendix A. Benchmark yield functions**

- von Mises isotropic model

$$\bar{\sigma}(\sigma) = \sqrt{\sigma_{xx}^2 + \sigma_{yy}^2 - \sigma_{xx}\sigma_{yy} + 3\sigma_{xy}^2}$$

- Hill 1948 anisotropic quadratic model

$$\bar{\sigma}(\sigma) = \sqrt{\frac{1}{2}\left((G+H)\sigma_{xx}^2 + (F+H)\sigma_{yy}^2 - 2H\sigma_{xx}\sigma_{yy} + 2N\sigma_{xy}^2\right)}$$

**Table A1. Anisotropic coefficients of Hill 1948 (AA6022-T4E32)**

| F | G | H | N |
|---|---|---|---|
| 1.3251 | 1.0730 | 0.8799 | 2.2014 |

- Yld2000-2d anisotropic non-quadratic model

$$\bar{\sigma}(\sigma) = (|X_1' - X_2'|^a + |2X_1'' + X_2''|^a + |X_1'' + 2X_2''|^a)^{1/a}$$

where $X_1'$, $X_2'$ are the principal values (eigenvalues) of the first linearly transformed stress tensor $\boldsymbol{X}'$, and $X_1''$, $X_2''$ are the principal values of the second transformed tensor $\boldsymbol{X}''$**.** The tensors $\boldsymbol{X}'$ and $\boldsymbol{X}''$ are defined as:

$$\boldsymbol{X}' = \begin{bmatrix} X_{xx}' \\ X_{yy}' \\ X_{xy}' \end{bmatrix} = \begin{bmatrix} L_{11}'\sigma_{xx} + L_{12}'\sigma_{yy} \\ L_{21}'\sigma_{xx} + L_{22}'\sigma_{yy} \\ L_{33}'\sigma_{xy} \end{bmatrix}, \qquad \boldsymbol{X}'' = \begin{bmatrix} X_{xx}'' \\ X_{yy}'' \\ X_{xy}'' \end{bmatrix} = \begin{bmatrix} L_{11}''\sigma_{xx} + L_{12}''\sigma_{yy} \\ L_{21}''\sigma_{xx} + L_{22}''\sigma_{yy} \\ L_{33}''\sigma_{xy} \end{bmatrix}$$

The linear transformation coefficients $L_{ij}'$ and $L_{ij}''$ are defined in terms of material anisotropy coefficients $\alpha_1$ through $\alpha_8$, as follows:

$$
\begin{aligned}
L'_{11} &= 2\alpha_1/3, & L''_{11} &= (8\alpha_5 - 2\alpha_3 - 2\alpha_6 + 2\alpha_4)/9 \\
L'_{12} &= -\alpha_1/3, & L''_{12} &= (4\alpha_6 - 4\alpha_4 - 4\alpha_5 + \alpha_3)/9 \\
L'_{21} &= -\alpha_2/3, & L''_{21} &= (4\alpha_3 - 4\alpha_5 - 4\alpha_4 + \alpha_6)/9 \\
L'_{22} &= 2\alpha_2/3, & L''_{22} &= (8\alpha_4 - 2\alpha_6 - 2\alpha_3 + 2\alpha_7)/9 \\
L'_{33} &= \alpha_7, & L''_{33} &= \alpha_8
\end{aligned}
$$

**Table A2. Anisotropic coefficients of Yld2000-2d (Ferritic Stainless-Steel type 409)**

| $\alpha_1$ | $\alpha_2$ | $\alpha_3$ | $\alpha_4$ | $\alpha_5$ | $\alpha_6$ | $\alpha_7$ | $\alpha_8$ | a |
|---|---|---|---|---|---|---|---|---|
| 0.9835 | 1.1182 | 0.7435 | 0.8517 | 0.8879 | 0.6511 | 0.9790 | 1.0810 | 6 |

## Appendix B. Spatiotemporally correlated Gaussian noise

To simulate realistic measurement uncertainty in the displacement field, we introduce additive Gaussian noise with spatial and temporal correlation. The noise is generated through a three-step procedure: (i) sampling uncorrelated Gaussian noise, (ii) temporal smoothing along the time axis, and (iii) spatial smoothing across nodes based on Euclidean distance.

Let $\bar{\eta}(\boldsymbol{x}, t)$ denote the initial uncorrelated noise sampled from $\mathcal{N}(0,1)$ at spatial node $\boldsymbol{x}$ and time step $t$. Temporal smoothing is first applied using a one-dimensional Gaussian kernel with standard deviation $\sigma_{time} = 5$ time steps (i.e., 5% of the total 100-step sequence):

$$\hat{\eta}(\boldsymbol{x}, t) = \sum_{\tau} G_{time}(t - \tau; \sigma_{time} = 5) \cdot \bar{\eta}(\boldsymbol{x}, \tau) \tag{B.1}$$

Next, spatial smoothing is performed independently for each time step. Given nodal coordinates $\{x_i\}_{i=1}^{m}$, the spatially correlated noise is computed as:

$$\eta(\boldsymbol{x}, t) = \sum_{j=1}^{m} w_{ij} \cdot \hat{\eta}(\boldsymbol{x}, t) \tag{B.2}$$

where the weights $w_{ij}$ are defined by a Gaussian kernel with spatial standard deviation

$\sigma_{space} = 5mm$:

$$w_{ij} = \frac{exp\left(-\frac{\left\|x_i - x_j\right\|^2}{2 * \sigma_{space}^2}\right)}{\sum_k exp\left(-\frac{\|x_i - x_k\|^2}{2 * \sigma_{space}^2}\right)} \tag{B. 3}$$

The smoothed noise is then normalized at each time step and displacement component to have zero mean and unit standard deviation:

$$\eta_{norm}(\boldsymbol{x}, t) = \frac{\eta(\boldsymbol{x}, t) - \mu_t}{\sigma_t} \tag{B. 4}$$

and scaled by a prescribed noise magnitude $\sigma_{\text{noise}}$ (in μm units):

$$\eta_{final}(\boldsymbol{x}, t) = \sigma_{\text{noise}} \cdot \eta_{norm}(\boldsymbol{x}, t) \tag{B. 5}$$

The final noisy displacement field is constructed as:

$$\boldsymbol{u_{noisy}}(\boldsymbol{x}, t) = \boldsymbol{u_{clean}}(\boldsymbol{x}, t) + \eta_{final}(\boldsymbol{x}, t) \tag{B. 6}$$

Three noise levels are considered—$\sigma_{\text{noise}} \in \{0.1\mu m, 0.2\mu m, 0.3\mu m\}$—to assess the robustness of the proposed framework under conditions representative of modern high-resolution DIC measurements.

## Reference


1. Simo, J. C. & Hughes, T. J. R. (1998). *Computational Inelasticity*. Springer.
2. de Souza Neto, E. A., Perić, D. & Owen, D. R. J. (2008). *Computational Methods for Plasticity: Theory and Applications*. Wiley.
3. Khan, A. S. & Huang, S. (1995). *Continuum Theory of Plasticity*. Wiley.
4. von Mises, R. (1913). Mechanik der festen Körper im plastisch deformablen Zustand. *Nachrichten der Gesellschaft der Wissenschaften zu Göttingen, Mathematisch-Physikalische Klasse*, 1913, 582–592.
5. Tresca, H. (1864). Mémoire sur l'écoulement des corps solides. *Comptes Rendus de l'Académie des Sciences de Paris*, 59, 754–758.
6. Drucker, D. C. (1959). A definition of stable inelastic material. *Journal of Applied Mechanics*, 26, 101–106.
7. Hill, R. (1948). A theory of the yielding and plastic flow of anisotropic metals. *Proceedings of the Royal Society A*, 193(1033), 281–297.
8. Barlat, F., Lege, D. J. & Brem, J. C. (1991). A six-component yield function for anisotropic materials. *International Journal of Plasticity*, 7(7), 693–712.
9. Barlat, F., Brem, J. C., Yoon, J. W. et al. (2003). Plane stress yield function for aluminum alloy sheets. Part I: Theory (Yld2000-2d). *International Journal of Plasticity*, 19(9), 1297–1319.
10. Barlat, F., Aretz, H., Yoon, J. W. et al. (2005). Linear transformation-based anisotropic yield function for aluminum alloy sheets (Yld2004-18p). *International Journal of Plasticity*, 21(5), 1009–1039.
11. Yoon, J. W., Barlat, F., Chung, K., Pourboghrat, F. & Yang, D. Y. (2000). Earing predictions based on asymmetric nonquadratic yield function. *International Journal of Plasticity*, 16(9), 1075–1104.
12. Yoon, J. W., Lou, Y., Yoon, J. & Glazoff, M. V. (2014). Asymmetric yield function based on the stress invariants for pressure-sensitive metals. *International Journal of Plasticity*, 56, 184–202.
13. Mu, Z., Zhao, J., Meng, Q., Zhang, Y. & Yu, G. (2022). Limitation analysis of the Hill48 yield model and establishment of its modified model for planar plastic anisotropy. *Journal of Materials Processing Technology*, 299, 117380.
14. Dasappa, P., Inal, K. & Mishra, R. (2012). The effects of anisotropic yield functions and their material parameters on prediction of forming limit diagrams. *International Journal of Solids and Structures*, 49(25), 3528–3550.
15. Fuhg, J. N., Anantha Padmanabha, G., Bouklas, N., Bahmani, B., Sun, W., Vlassis, N. N. et al. (2024). A review on data-driven constitutive laws for solids. *Archives of Computational Methods in Engineering*, 1–43.
16. Hussain, A., Sakhaei, A. H. & Shafiee, M. (2024). Machine learning–based constitutive modelling for material nonlinearity: A review. *Mechanics of Advanced Materials and Structures*.
17. Mozaffar, M., Bostanabad, R., Chen, W., Ehmann, K., Cao, J. & Bessa, M. A. (2019). Deep learning predicts path-dependent plasticity. *Proceedings of the National Academy of Sciences of the USA*, 116(52), 26414–26420.
18. Li, X., Roth, C. C. & Mohr, D. (2019). Machine-learning based temperature- and rate-dependent plasticity model. *International Journal of Plasticity*, 120, 11–27.
19. Jang, D. P., Fazily, P. & Yoon, J. W. (2021). Machine learning–based constitutive model for J2-plasticity. *International Journal of Plasticity*, 138, 102919.

20. Fazily, P. & Yoon, J. W. (2023). Machine learning–driven stress integration method for anisotropic plasticity in sheet metal forming. *International Journal of Plasticity*, 166, 103642.
21. Heidenreich, J. N. & Mohr, D. (2024). Recurrent neural network plasticity models: Unveiling their common core through multi-task learning. *Computer Methods in Applied Mechanics and Engineering*, 426, 116991.
22. Heidenreich, J. N. & Mohr, D. (2025). Extended minimal state cells (EMSC): Self-consistent recurrent neural networks for rate- and temperature-dependent plasticity. *International Journal of Plasticity*, 188, 104305.
23. Wang, K. & Sun, W. (2019). Meta-modeling game for theory-consistent microstructure-based constitutive models via deep reinforcement learning. *Computer Methods in Applied Mechanics and Engineering*, 337, 267–286.
24. Vlassis, N. N. & Sun, W. (2021). Sobolev training of thermodynamic-informed neural networks for interpretable elasto-plasticity models. *Computer Methods in Applied Mechanics and Engineering*, 380, 113818.
25. Meyer, K. A. & Ehret, F. (2023). Thermodynamically consistent neural network plasticity modeling and discovery of evolution laws. *Journal of the Mechanics and Physics of Solids*, 169, 105324.
26. Kabliman, E., Kolody, A. H., Kronsteiner, J., Kommenda, M. & Kronberger, G. (2021). Application of symbolic regression for constitutive modeling of plastic deformation. *Applications in Engineering Science*, 6, 100052.
27. Bahmani, B., Suh, H. S. & Sun, W. (2024). Discovering interpretable elastoplasticity models via the neural polynomial method enabled symbolic regressions. *Computer Methods in Applied Mechanics and Engineering*, 422, 116827.
28. Bomarito, G., Townsend, S., Stewart, K., Esham, K., Emery, J. & Hochhalter, J. (2021). Interpretable data-driven plasticity models with symbolic regression. *Computers & Structures*, 246, 106482.
29. Flaschel, M., Kumar, S. & De Lorenzis, L. (2022). Discovering plasticity models without stress data. *npj Computational Materials*, 8, 21.
30. Flaschel, M., Kumar, S. & De Lorenzis, L. (2023). Automated discovery of generalized standard material models with EUCLID. *Computer Methods in Applied Mechanics and Engineering*, 391, 114634.
31. Xu, H., Flaschel, M. & De Lorenzis, L. (2025). Discovering non-associated pressure-sensitive plasticity models with EUCLID. *Advanced Modeling and Simulation in Engineering Sciences*, 12(1), 1.
32. Ghnatios, C., Cazacu, O., Revil-Baudard, B. & Chinesta, F. (2024). A new methodology for anisotropic yield surface description using model order reduction techniques and invariant neural network. *Journal of the Mechanics and Physics of Solids*, 184, 105542.
33. Soare, S. C. (2025). On the use of neural networks in the modeling of yield surfaces. *International Journal for Numerical Methods in Engineering*, 126(1), e7616.
34. Amos, B., Xu, L. & Kolter, J. Z. (2017). Input convex neural networks. In *Proceedings of the 34th International Conference on Machine Learning*, 146–155.
35. Flaschel, M., Steinmann, P., De Lorenzis, L. & Kuhl, E. (2025). Convex neural networks learn generalized standard material models. *Journal of the Mechanics and Physics of Solids*, 200, 106103.

36. Ghouli, S., Flaschel, M., Kumar, S. & De Lorenzis, L. (2025). A topology optimisation framework to design test specimens for one-shot identification or discovery of material models. *Journal of the Mechanics and Physics of Solids*, 165, 106210.
37. Tung, C. H. & Li, J. (2024). The anti-dogbone: Evaluating and designing optimal tensile specimens for deep learning of constitutive relations. *Extreme Mechanics Letters*, 69, 102157.
38. Pierron, F., Avril, S. & Tran, V. T. (2010). Extension of the virtual fields method to elasto-plastic material identification with cyclic loads and kinematic hardening. *International Journal of Solids and Structures*, 47(22–23), 2993–3010.
39. Marek, A., Davis, F. M., Rossi, M. & Pierron, F. (2019). Extension of the sensitivity-based virtual fields to large deformation anisotropic plasticity. *International Journal of Material Forming*, 12(3), 457–476.
40. Soare, S., Yoon, J. W. & Cazacu, O. (2008). On the use of homogeneous polynomials to develop anisotropic yield functions with applications to sheet forming. *International Journal of Plasticity*, 24(6), 915–944.
41. Soare, S. & Barlat, F. (2010). Convex polynomial yield functions. *Journal of the Mechanics and Physics of Solids*, 58(11), 1804–1818.
42. Soare, S. C. & Diehl, M. (2024). Calibration and fast evaluation algorithms for homogeneous orthotropic polynomial yield functions. *Computational Mechanics*, 73(6), 1219–1239.